Quantitative Resolution of Complex Stoichiometric Changes During Electrochemical Cycling by Density Functional Theory Assisted, Electrochemical Quartz Crystal Microbalance

Tzu-Ho Wu[†,‡,ǁ,Ⅱ], Ivan Scivetti*[‡,§,Ⅱ], Jia-Cing Chen[†], Jeng-An Wang[†], Gilberto Teobaldi[‡,⌘,ʃ], Chi-Chang Hu*[,†], and Laurence J. Hardwick*[,‡]

†Department of Chemical Engineering, National Tsing Hua University, Hsin-Chu, 30013 TAIWAN

‡Department of Chemistry, Stephenson Institute for Renewable Energy, The University of Liverpool, Crown Street, Liverpool, L69 7ZD, UK

ǁDepartment of Chemical & Materials Engineering, National Yunlin University of Science and Technology, Yunlin, 64002, TAIWAN

§Scientific Computing Department, Science and Technology Facilities Council, Daresbury Laboratory, Keckwick Lane, Daresbury, WA4 4AD, Warrington, UK

⌘Scientific Computing Department, Science and Technology Facilities Council, Rutherford Appleton Laboratory, Harwell Campus, OX11 0QX Didcot, UK

ʃBeijing Computational Science Research Center 100193 Beijing, China

Ⅱ These Authors contributed equally to the manuscript

*Corresponding Author: Ivan Scivetti

E-mail: ivan.scivetti@stfc.ac.uk

*Corresponding Author: Chi-Chang Hu, NTHU Chair Professor

Phone & Fax: +886-3-5736027

E-mail: cchu@che.nthu.edu.tw

Website: http://mx.nthu.edu.tw/~cchu/

*Corresponding Author: Laurence J. Hardwick

E-mail:hardwick@liverpool.ac.uk

Abstract

The capability to simultaneously measure changes of mass and charge of electroactive materials during a redox process makes Electrochemical Quartz Crystal Microbalance **(EQCM)** a powerful technique to monitor stoichiometric changes during reversible electrochemical processes. In principle, quantitative resolution of the stoichiometry of the electroactive sample during electrochemical cycling can be obtained by solving the system of equations for the EQCM mass and charge balance. Such system of equations couples the measured changes in mass and charge through the stoichiometry of the redox process. Unfortunately, whenever more than two chemically inequivalent species are involved in the redox process, the system of equations is mathematically undetermined, having more variables (stoichiometric coefficients) than equations. In these cases, current best practice is the arbitrary reduction of the number of variables in the mass and charge balance equation, by using chemical intuition to set some of the stoichiometric coefficients to fixed values. For layered ion-intercalation host materials, widespread practical approximations are the use of arbitrarily defined solvation numbers for the intercalating ions or the neglect of ion-induced displacement of structural solvent inside the host. Here, we propose an alternative approach based on the use of Density Functional Theory **(DFT)** to sample and screen, on an energy basis, the whole *unreduced* spectrum of stoichiometric coefficients compatible with EQCM measurements, leading to DFT energy-assisted resolution of stoichiometric changes during cycling. We illustrate the approach by taking nickel hydroxide $Ni(OH)_2$ as a case system and studying its ion-intercalation-driven phase transformations in the presence of different LiOH,

NaOH, and KOH electrolytes. Quantitative resolution of the $Ni(OH)_2$ stoichiometry during electrochemical cycling unambiguously reveals ion-intercalation to displace structural water from the layered host, promoting electrochemical degradation and aging of the material. The process is found to be strongly dependent on the size of the electrolyte cation, with larger cations displacing larger amounts of structural water and resulting in faster degradation rates.

KEYWORDS

Electrochemical Quartz Crystal Microbalance; Density Functional Theory; nickel hydroxide; *In situ* Raman spectroscopy; ion-intercalation; structural water; electrochemical degradation

1. INTRODUCTION

Reversible, electrochemical ion intercalation into a host material is one of the fundamental processes available for electrochemical energy storage and conversion.[1-3] The efficiency (and reversibility) of such a process is ruled not only by the way ions intercalate, but also by the structural response of the host material. Although this complex interplay has been extensively studied for many decades,[3] a deeper understanding of the fundamental mechanisms is required for the implementation of improved solutions of existing battery technologies and the rational design of new materials for future energy applications.

The capability to simultaneously measure changes of mass and charge of electroactive materials during the redox process makes Electrochemical Quartz Crystal Microbalance (**EQCM**)[4-8] a powerful technique to gain quantitative atomistic insights into redox processes. Interpretation of EQCM measurements is possible, in principle, via the mass and charge balance equations that couple the measured changes in mass and charge with the stoichiometry of the redox process. Analytically, the number of independent variables in this system of equations depends on the proposed stoichiometry of the redox process. Thus, if the stoichiometry of the redox process involves more than two chemically different species, the system of the (two) mass and charge balance equations contains more independent variables (the stoichiometric coefficients) than equations and is, as a result, *underdetermined*. Consequently, and perhaps unfortunately, whenever the stoichiometry of the redox process involves

more than two chemically different species, their stoichiometric coefficients cannot be unequivocally determined by solving the system of equations for the balance of the EQCM-measured mass and charge changes.

This shortcoming is routinely bypassed by *arbitrarily* reducing the number of independent variables (the stoichiometric coefficients) in the mass and charge balance equation using chemical intuition. In the case of ion intercalation into layered host materials, widespread practical approximations are the use of *chemically educated* guesses on the degree of solvation for the intercalated cations inside the host based on bulk solvent-phase estimates and/or the neglect of possible changes in structural solvent contained in the host material.[5] However, to the best of our knowledge, the validity of these approximations has never been corroborated quantitatively in the available literature neither experimentally nor computationally. This in turn legitimates doubts on their quantitative value and, inevitably, interpretation of EQCM data. Prompted by these considerations, here we scrutiny current best practice in the interpretation of EQCM measurements, and propose an alternative approach based on **i)** the substitution of chemical intuition by computation of Density Functional Theory (**DFT**) formation energies, and **ii)** the use of DFT to screen, on an energy basis, the whole *unreduced* spectrum of stoichiometries compatible with EQCM measurements. In spite of its simplicity, to the best our knowledge, such approach is unprecedented in the available EQCM literature.

As a case-system, we focus on nickel hydroxide, $Ni(OH)_2$, and revisit, via EQCM and complementary approaches, the electrochemical intercalation of alkali metal ions (Li^+, Na^+ and K^+). $Ni(OH)_2$ is a layered material that provides the typical environment for ion (de)intercalation via redox reactions, and has been studied for a variety of electrochemical applications, including nickel-based batteries,[9-11] supercapacitors,[12-14] electrochromic devices[15-17] and electrocatalysts.[18-20] Redox transitions for this material are generally described with the diagram of **Figure 1a**, typically referred to as the Bode diagram.[8, 21]

Two phases α (violet, bottom) and β (orange, bottom) are found for $Ni(OH)_2$. The α phase is composed of disordered nickel hydroxides with randomly oriented layers, separated by intercalated water molecules/ions.[22] In contrast, the β phase is thermodynamically more stable, and exists in nature as theophrastite mineral with a layered structure free of intercalated water. These α and β $Ni(OH)_2$ phases are understood to be oxidized (upon charging) to γ-$Ni(OH)_2$ (green) and β-NiOOH (lighter orange, top) phases, respectively. This in turn defines two possible redox couples: γ-$Ni(OH)_2$/α-$Ni(OH)_2$ and β-NiOOH/β-$Ni(OH)_2$. Although, in principle, γ-$Ni(OH)_2$ could also be formed by overcharging of the β-NiOOH phase, the large differences in the inter-slab distances between the two phases (4.8 Å for β-NiOOH vs. 7 Å for γ-NiOOH) leads to large mechanical deformations and subsequent material degradation in contrast to the γ-NiOOH/α-$Ni(OH)_2$ couple. In addition, the change of average nickel oxidation state between γ-NiOOH/α-$Ni(OH)_2$ indicates this redox reaction involves transfer of more

than one electron per Ni atom, while the β-NiOOH/β-$Ni(OH)_2$ undergoes transfer of only one electron during the redox process. Thus, the β-NiOOH/β-$Ni(OH)_2$ couple exhibits lower charge capacity in comparison with the γ-NiOOH/α-$Ni(OH)_2$,[8, 23] and the α-$Ni(OH)_2$ phase is usually preferred for energy storage applications (e.g., rechargeable batteries and asymmetric supercapacitors).[14, 23, 24] Unfortunately, the reversibility of the γ-NiOOH/α-$Ni(OH)_2$ redox couple is compromised by a gradual conversion of α-$Ni(OH)_2$ to β-$Ni(OH)_2$ during either consecutive potential cycling[25] or treatment in highly concentrated electrolytes (6M KOH at 50 °C)[26]. This process is commonly referred to as 'aging' in the literature.[27, 28] The far from conclusive understanding of the atomistic mechanisms of this degradation process prevents definition of viable strategies to stabilize α-$Ni(OH)_2$ and, ultimately, take up of the substrate as technologically viable material for energy storage applications.

To reduce this knowledge gap, here, we present a simple, yet to date unprecedented approach to quantitatively interpret the evolution of α-$Ni(OH)_2$ during the initial stages of electrochemical cycling. DFT-energy based screening of the stoichiometries compatible with the EQCM measurements reveals an unexpected role for intercalated alkali ions in displacing the structural water molecules from the layered host structure, promoting the irreversible collapse of the α-$Ni(OH)_2$ phase into β-$Ni(OH)_2$. EQCM, *in situ* Raman and DFT results demonstrate that the degradation rate of α-$Ni(OH)_2$ is directly related to the size of the intercalated ion, with larger ions displacing larger amount of water, thus accelerating the α-$Ni(OH)_2$ to β-$Ni(OH)_2$ aging process.

More generally, we believe our combined EQCM-DFT (transferable) approach for quantitative resolution of the stoichiometry of electroactive materials during cycling constitutes a beneficial addition to the set of tools currently used for fundamental research in electrochemical energy storage.

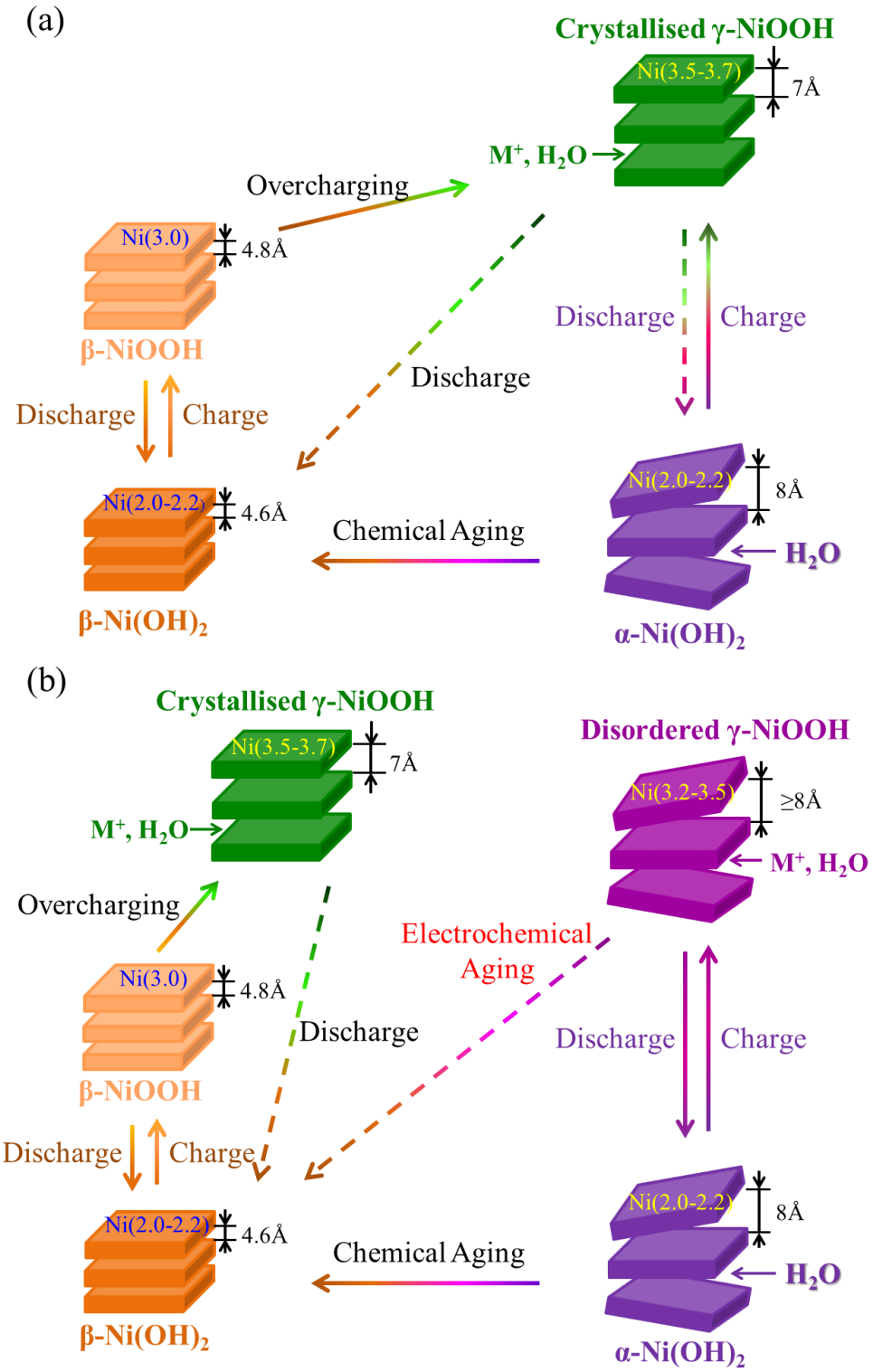

Figure 1 (a) Bode diagram revealing the correlations between various phases of $Ni(OH)_2$ (b) Proposed modification of the Bode diagram with the disordered γ-$Ni(OH)_2$ phase obtained from the oxidation of α-$Ni(OH)_2$. Numbers in parenthesis indicate the average oxidation state for nickel.

2. EXPERIMENTAL AND COMPUTATIONAL DETAILS

2.1. Experimental setup

For EQCM measurements, nickel hydroxide samples were prepared by cathodic deposition from a bath consisting of 40 mM $NaNO_3$ and 20 mM $NiCl_2 \cdot 6H_2O$ onto Au/Ti-sputtered quartz crystal (CHI125A, CH Instruments Inc.) at room temperature. Further EQCM experimental parameters can be found within Section 7 of the Supporting Information. The cathodic current for $Ni(OH)_2$ deposition was fixed to 20 µA for 500 s. Samples were vacuum dried overnight before EQCM measurements. EQCM experiments were carried out for 20 cycles by varying the potential between 0 and 0.45 V. To identify and quantify the role of kinetics effects in the electrochemical cycling of the materials, we used a voltage scan rate of 5 mV s^{-1} for the first 10 cycles and 10 mV s^{-1} for the following 10 cycles. The reference and counter electrodes were Ag/AgCl (Argenthal, 3 M KCl, 0.207 V versus SHE at 25 ^{o}C) and a platinum wire, respectively. All the EQCM responses were measured by an electrochemical analyzer (CHI4053a, CH Instruments Inc.) The alkaline electrolytes were LiOH (TEDIA, USA), NaOH (SHOWA, Japan), and KOH (SHOWA, Japan) in one molar (1 M) concentration. All solutions used in this work were prepared with deionized water produced by a reagent water system (Milli-Q SP, Japan) at 18 MΩ cm. The alkaline electrolytes used for electrochemical characterization was degassed with purified N_2 for 25 min before measurements.

The as-deposited α-$Ni(OH)_2$ powders were collected from a graphite electrode surface (Nippon Carbon EG-NPL, N.C.K.) after cathodic deposition. The pretreatment of graphite electrodes followed

the protocol of previous work[29]. The formation of α phase was corroborated by powder X–ray diffraction (PXRD) (CuKα, Ultima IV, Rigaku) (Figure S1 of the SI). Thermal properties were analyzed by thermogravimetric analysis (TGA, SDT Q600, TA Instruments) with a heating rate of 5 ^{o}C min^{-1} in N_2 atmosphere (Figure S5).

In situ Raman spectra were recorded with a Raman microscope (Renishaw inVia), using a He-Ne laser (632.8 nm) focused through an inverted microscope (Leica) via a 50× objective lens (Leica). Chemically synthesized $Ni(OH)_2$ was prepared[30] and characterized as α-$Ni(OH)_2$ by PXRD (Figure S1b) and Raman (Figure S20) experiments. Then, the material was cast onto a nickel electrode for *in situ* Raman experiments. Again, we used Ag/AgCl (Argenthal, 3 M KCl, 0.207 V versus SHE at 25 ^{o}C) as the reference electrode and a platinum wire as the counter electrode. *In situ* Raman spectra were recorded every 10 cyclic voltammetry (CV) cycles at rest condition (i.e., without applied voltage) just after potential cycling (10 mV s^{-1}) between 0 and 0.45 V in the three alkaline electrolytes described above. For each spectrum, the acquisition time is 50 s in the range of 3400–3800 cm^{-1} with five accumulations. Via an appropriate filtering, the power of the laser was set below 3.7 mW.

2.2. Computational methods

All the DFT simulations were spin-polarized using the projector augmented wave method[31] together with periodic boundary conditions (PBCs) as implemented in the VASP code.[32-34] Following previous computational work on the phase stability of nickel hydroxides and oxyhydroxides,[35] the electronic exchange-correlation was treated according to the GGA-PW91 approximation[36] with the interpolation formula of Vosko *et. al.*[37] To improve the description of Ni *3d* electrons, we used the DFT+U method[38-41] with the Hubbard Coulomb term U spherically averaged[42] and equal to 6.0 eV, whereas the exchange term *J* was set to zero. Based on the benchmark calculations of J. Zaffran *et. al.*,[43] we did not included van der Waals corrections. All the calculations were carried out assuming ferromagnetic ordering. We have used 550 eV for the plane-wave energy cutoff. The Brillouin zone sampling was based on the Monkhorst-Pack scheme.[44] Images of the simulated models have been created with the VESTA visualization program.[45] Further details are provided in Section S8 of the Supporting Information (SI).

3. RESULTS AND DISCUSSION

3.1. *In situ* Raman evolution of $Ni(OH)_2$

In situ Raman spectroscopic experiments were first carried out to investigate the phase evolution of α-$Ni(OH)_2$ with cycling. The Raman spectrum of the pristine $Ni(OH)_2$ sample (bottom black curves in Figure 2) exhibits a band intensity in the range of 3550-3680 cm^{-1}, which corresponds to the turbostratic α phase.[46, 47] The broad responses can be fitted by convolution of Lorentzian functions centred at 3590, 3620, 3645, and 3665 cm^{-1} (Figure S22a, Table S8), which are related to O-H vibrational mode of lattice OH and structural water inside α-$Ni(OH)_2$ host.[47, 48] Based on the fitting results, the 3620 cm^{-1} peak has the strongest intensity among them, which is later used as an indicator of α-$Ni(OH)_2$. After 10 cycles in LiOH (Figure 2a), there are no qualitative differences with respect to the pristine sample, indicating that the β-$Ni(OH)_2$ phase cannot be observed via Raman at this stage. On the other hand, the subtle changes of Raman spectra obtained in NaOH (Figure 2b) and KOH (Figure 2c) can be convoluted by Lorentzian peak fitting (Figure S22d and S22e), as the peak at 3580 cm^{-1} corresponding to A_{1g} O−H stretching mode of β-$Ni(OH)_2$ emerges.[30, 46] The intensity ratio (I_β/I_α) between the most representative peaks of β (3580 cm^{-1}) and α-$Ni(OH)_2$ (3620 cm^{-1}) is introduced to provide quantitative information on the phase transformation from α to β-$Ni(OH)_2$ over CV cycling. The I_β/I_α of $Ni(OH)_2$ in NaOH and KOH after 10 CV cycles is determined as 0.33 and 0.35, respectively. The results indicate the α-$Ni(OH)_2$ undergoes electrochemical aging within the first 10 CV cycles in NaOH and KOH, but not in LiOH. As for 30 cycles in KOH (Figure 2c), the β-$Ni(OH)_2$ responses become more prominent, and the most intense

peak is at 3580 $cm^{-1}$with I_β/I_α increased to 1.85. The peak at 3601 cm^{-1} has been assigned to $\upsilon_{(O-H)}$ in disordered β-$Ni(OH)_2$,[27, 46] which is commonly found in electrochemically induced β-$Ni(OH)_2$ from repeated CV cycling of the α phase, presumably owing to the residual cations and water molecules inside the structure. In contrast, for both LiOH (I_β/I_α = 0.35) and NaOH (I_β/I_α = 0.40) the peak at 3580 cm^{-1} also manifests but with a much lower intensity. Upon further cycling to 150 cycles, the I_β/I_α drastically increases to 2.24 and 5.42 for NaOH and KOH, indicating predominant β-$Ni(OH)_2$ presence in the sample for both electrolytes at this stage. Conversely, the β-$Ni(OH)_2$ signals in LiOH displays a much lower intensity (I_β/I_α = 0.49). The predominant presence of β-$Ni(OH)_2$ can be observed in LiOH after 200 cycles, although the I_β/I_α for LiOH (1.81) is lower than that of NaOH (3.86) and KOH (5.45). Complementary Raman results are reported in Section S11 of the SI.

Based on the *in situ* Raman results, the starting material, α-$Ni(OH)_2$, undergoes electrochemical aging process leading to gradual formation of β-$Ni(OH)_2$ in the electrode. These findings demonstrate a variation in the transformation from the α to β phase that is dependent on the alkali metal cation used within the electrolyte. With larger size of electrolyte cation, the degradation rate is faster. In addition, careful analysis of the Raman spectra highlights the coexistence of both the α and β phases during repeated CV cycling, which is in agreement with previous work.[7, 49]

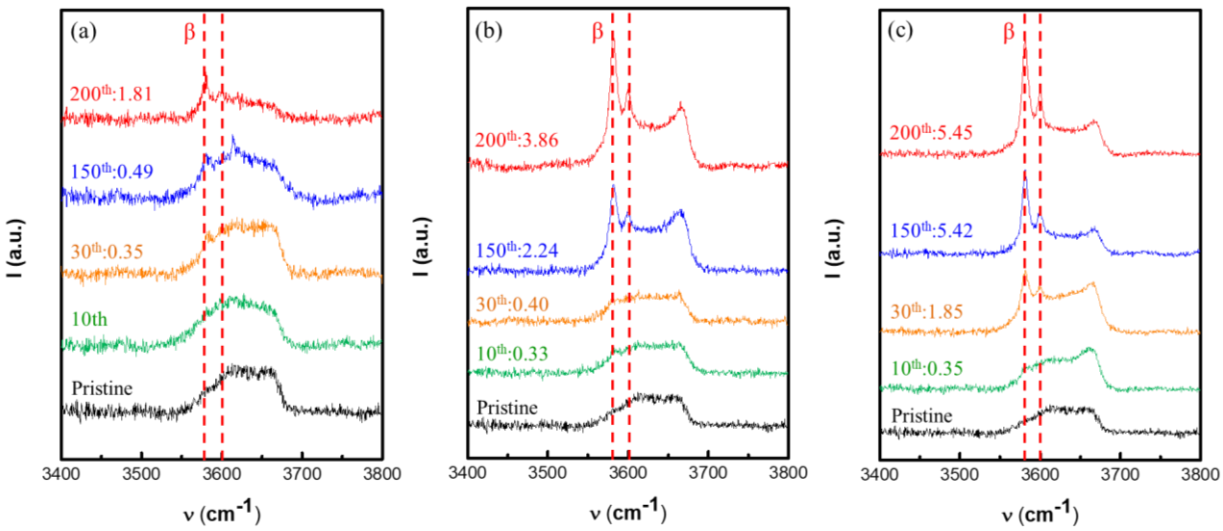

Figure 2 *In situ* Raman spectra of $Ni(OH)_2$ recorded after 10, 30, 150, and 200 CV cycles at 10 mV s^{-1} in 1 M (a) LiOH, (b) NaOH, (c) and KOH. The additional numeric labels (0.33-5.45 range) in the figures reports the intensity ratio (I_β/I_α) between the most representative peaks of the Lorentzian functions used for the β and α-$Ni(OH)_2$ phases. Raman spectra with detailed fitting curves are shown in section S11 of the SI.

Although the *in situ* Raman results provide informative characterization of the material and its changes upon CV cycling, they offer no direct quantitative insights into the stoichiometric changes and atomistic mechanisms involved in the degradation of the α-$Ni(OH)_2$ phase. However, as we show below, such quantitative insights can be provided by (DFT) energy screening of the whole spectrum of stoichiometric solutions compatible with the EQCM measurements via the mass and charge balance equations.

3.2 Determination of the stoichiometry for the as-prepared α-$Ni(OH)_2$ film

We prepared the α-$Ni(OH)_2$ film by cathodic deposition at room temperature. The diffraction pattern of the as-prepared material (Figure S1a) can be correlated to the PXRD pattern of α-$Ni(OH)_2$ from the

database (JCPDS CARD 22-0444). Thus, the pristine material for the EQCM studies is characterized as α-$Ni(OH)_2$.

Ahead of the EQCM study of the evolution of α phase with electrochemical cycling, we focus on the stoichiometry of the as-prepared, electrochemically deposited, α-$Ni(OH)_2$ film. From combined thermogravimetric analysis (TGA) and DFT simulations (Section S5 of SI) we determine a unitary stoichiometric coefficient for the structural water inside the α-$Ni(OH)_2$ layers, in the absence of any intercalated cation. Thus, we determine that the formula unit for the α phase is α-$Ni(OH)_2(H_2O)$, which is in agreement with previous findings in the literature.[50] It is important to remark this result contradicts the assumption of no intercalated H_2O in the pristine α phase (i.e., α-$Ni(OH)_2$) used in a seminal EQCM study of this material.[5]

3.3 γ/α redox couple

Extensive research in electrochemical oxidation of α-$Ni(OH)_2$ has resulted in proposition of several different intercalation mechanisms, depending on the chemical nature of the cation in the electrolyte and its pH[8]. Based on the chemical reaction proposed in literature[5], we assume that oxidation reaction (charging) of the α phase into the γ one involves *x* water molecules (H_2O), *y* electrolyte cations (M^+ = Li^+, Na^+ or K^+), and *z* protons (H^+) as follows:

$$\alpha[Ni(OH)_2(H_2O)] + yM^+(H_2O)_{x/y} + (2-z)OH^- \rightarrow$$

$$\gamma[M_yH_z(H_2O)_{1+x}NiO_2] + (2-z)(H_2O) + (2-z-y)e^- \qquad (1)$$

The stoichiometric coefficient *x*, *y*, and *z* in (1) are related via the mass (Δm_{ox}) and charge (Q_{ox}) change balance equations:

$$\Delta m_{ox} = n[yAW_{M^+} + xMW_{H_2O} - (2-z)AW_{H^+}] \quad (2)$$

$$Q_{ox} = nF(2-z-y) \quad (3)$$

Δm_{ox} and Q_{ox} in Eqs. (2)-(3) are measured by EQCM during the oxidation process (See Fig S6). AW_{M^+} and AW_{H^+} are the atomic weights of cations (M^+) and protons (H^+), respectively. MW_{H_2O} is the molecular mass of water. *F* is the Faraday constant, and *n* is total number of moles (of the pristine α phase) involved in the reaction.

Under the assumption that $Ni(OH)_2(H_2O)$ is the only product formed during galvanostatic deposition, and that the whole deposited film participates in the reaction, *n* can be calculated from the EQCM mass (m_f) of the electrochemically deposited α-$Ni(OH)_2(H_2O)$ film (of molecular weight $MW_{[Ni(OH)_2(H_2O)]}$) as:

$$n = \frac{m_f}{MW_{[Ni(OH)_2(H_2O)]}}. \quad (4)$$

Before proceeding, we reiterate that owing to the presence of intercalated water in α-$Ni(OH)_2(H_2O)$, neglected in Ref. [5] and affecting the number of α-phase moles actually deposited, the system of equations (2)-(3) is bound to provide results different from assuming no intercalated water as postulated in Ref. [5]. In the following, we quantify such deviations.

Having three independent variables (*x*, *y*, and *z*) the system of two linear equations (2)-(3) is mathematically *underdetermined*. This results in an *infinite* number of possible solutions for the stoichiometric coefficient of water (x) and its ratio to cation content (*x/y*) as a function of the value of *z* (stoichiometric coefficient for protons in Eqn. 1). For this reason, quantitative interpretation of EQCM experiments can only be put forward based on chemically educated assumptions that enable setting one of the three independent variables (*x*, *y*, and *z*) to a fixed value, leaving a system of two equations for two variables. For example, Cordoba-Torresi *et al.*[5] used the information on bulk-phase solvation number for cations to set the (*x/y*) ratio equal to 3 and 1 for inserted Li^+ and K^+, respectively. This assumption, in turn, enabled determination of the remaining *y* and *z* coefficients, thence redox stoichiometry, based on the acquired EQCM data and Eqn. (2)-(4).[5] However, the evidently different local environment for the cations of the electrolyte between the $Ni(OH)_2$ layers and in the bulk-solvent region (Eq. 1) raises legitimate questions about the correctness of this assumption, prompting further (DFT-energy based) scrutiny, which we provide in the next sections.

3.4 β-NiOOH/β-$Ni(OH)_2$ redox couple

In contrast to the α phase, β-$Ni(OH)_2$ undergoes intercalation/de-intercalation of protons through a simpler redox reaction process:

$$\beta[Ni(OH)_2] \leftrightarrows \beta[NiOOH] + H^+ + e^- \qquad (5)$$

with a small change of the interlayer distance (see Fig 1a). Previous EQCM experiments for $Ni(OH)_2$ show that the γ/α redox couple exhibits an opposite mass change response with respect to β-$Ni(OH)_2$/β-NiOOH.[4-8] For the former, the intercalation of external cations from the electrolyte into $Ni(OH)_2$ host structure during oxidation leads to mass increase, following a mass decrease from cation de-intercalation during reduction. Conversely, protons removed from β-$Ni(OH)_2$ during oxidation lead to a mass decrease of the host electrode, followed by a mass increase when proton are (re)-intercalated into β-NiOOH upon reduction.

3.5 Electrochemical and EQCM characterization

Figure 3a shows the CV measurements for the pristine α phase deposited on the EQCM electrodes for the first cycle. The CV profiles exhibit the typical voltammetric response of the γ/α redox couple with well-defined electrolyte dependent redox peaks at ca. 0.35 and 0.25 V (vs. Ag/AgCl), respectively. The order of cations with respect to position of the oxidation peak potential is $Li^+ > Na^+ \approx K^+$. We attribute the positive shift of the peak in 1 M LiOH with respect to NaOH and KOH to a Nernstian potential-pH effect. In fact, previous experiments demonstrate that the concentration of OH^- plays an important role on the redox behavior of the γ/α couple.[51] Here, we attribute these differences to a relatively lower pH of the 1 M LiOH solution in comparison with 1 M NaOH and KOH electrolytes (**Section S2 of the SI**).

The corresponding mass change profiles (Δ*m*-*E*) are shown in **Figure 3b**. The onset of the mass gain is at ca. 0.32 V in the positive sweep for the oxidation of the α phase into the γ one.[5-7] In contrast, mass loss is observed at ca. 0.28 V during reduction. The order of electrolytes with respect to decreasing the mass change in the redox process is KOH > NaOH > LiOH. This trend correlates to the atomic weight of cations (i.e., $K^+ > Na^+ > Li^+$), in agreement with the work of G. T. Cheek and W. E. O'Grady [52]. However, this trend is different from the findings of Cordoba-Torresi *et al.*[5] and Bernard *et al.*[53], where the mass uptake during oxidation is found to be practically independent of the cation species. Unfortunately, we are unable to unambiguously explain the origin of such a stark qualitative difference. One can only speculate that they may be attributed to differences in sample preparation and/or EQCM setup. As further elaborated in the **SI** (**discussion of Figure S9)**, we suggest that EQCM-derived Δm/ΔQ calibrations could be very meaningfully started to be used as unambiguous fingerprints for the deposited electroactive material. This in turn would greatly benefit future comparison and discussion of independent experiments and results on *expectedly* the same material.

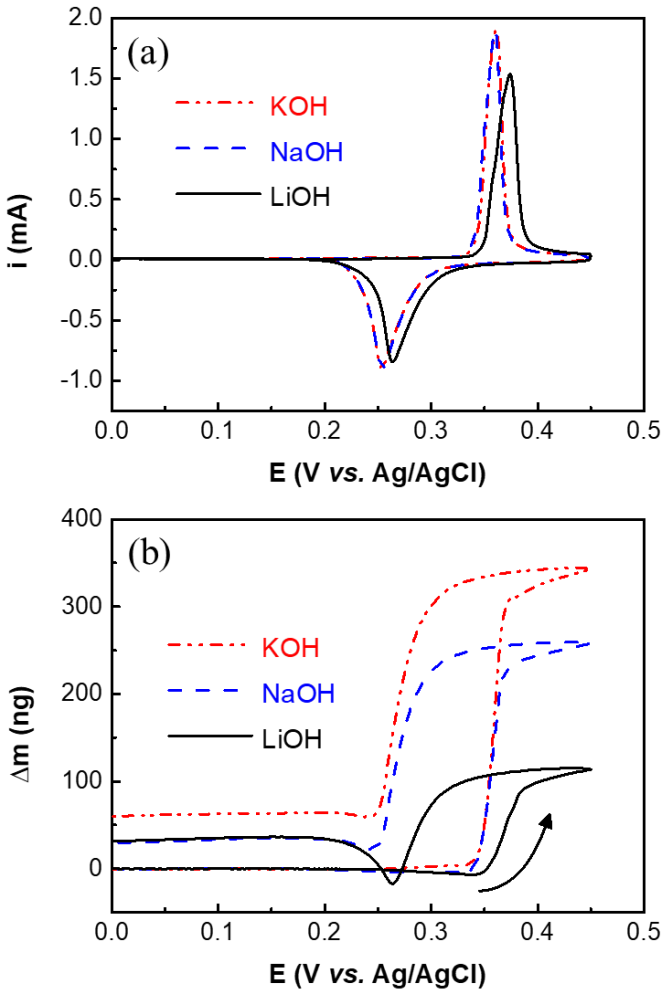

Figure 3 (a) cyclic voltammograms and (b) mass change profiles of α-$Ni(OH)_2(H_2O)$ deposited on the EQCM gold electrodes during the first cycle in 1 M LiOH, NaOH and KOH (scan rate: 5 mV s^{-1}).

The role of the electrolyte cation for the details of the electrochemical aging is unambiguously revealed by the EQCM-measured (Δm–E) traces under continuous potential cycling. **Figure 4** shows both CV and mass change profiles for selected cycles at 10 mV s^{-1} following 10 initial cycles. For the LiOH electrolyte (Figures 4a and 4d), the EQCM profiles exhibit the typical response of the γ/α redox couple although the magnitude of the current (**Figure 4a**) and the mass peaks (**Figure 4d**) slightly decrease with cycling. For NaOH and KOH (**Figures 4b and 4c**), the reduction and oxidation peak currents remain consistent between CV 11th and 20th cycle. Conversely, the mass change profiles (**Figures 4e**

and 4f) show a drop followed by the gain of mass during the oxidation of the α phase from 0.35 to 0.38 V on the positive sweeps, which is attributed to the oxidation of β-$Ni(OH)_2$ to β-NiOOH during which protons are removed, as shown in Eqn. (5).[6] The reduction of β-NiOOH is manifested by a minor mass gain at ca. 0.27 V due to the insertion of proton. Such a mixed electrochemical response demonstrates the coexistence of the γ/α and β/β redox couples that are found to start at 6^{th} cycle (NaOH) and 7^{th} cycle (KOH), see **Figure S3 in the SI**. In contrast to LiOH, we obtain a net mass gain upon CV cycling, ca. 12 and 17.5 ng per CV cycle for NaOH and KOH, respectively, suggesting that intercalated Na^+ and K^+ ions are not fully removed from the host structure during reduction, thus increasing the amount of residual mass at the end of each CV cycle. EQCM results were also investigated by massograms, which reports the rate of mass change ($d\Delta m/dt$) as a function of the electrode potential (Figure S2). In LiOH, we observe a pair of peaks (one for charge and one for discharge) characteristic of the γ/α redox transition. In contrast, we observe two pairs of peaks (two for charging and two for discharging) when cycling the samples in NaOH and KOH, which indicate the coexistence of the γ/α to β/β redox couples. In addition, while the magnitude of the peaks corresponding to the γ/α transition decreases with the cycles, the opposite is observed for the β/β response, thus demonstrating the

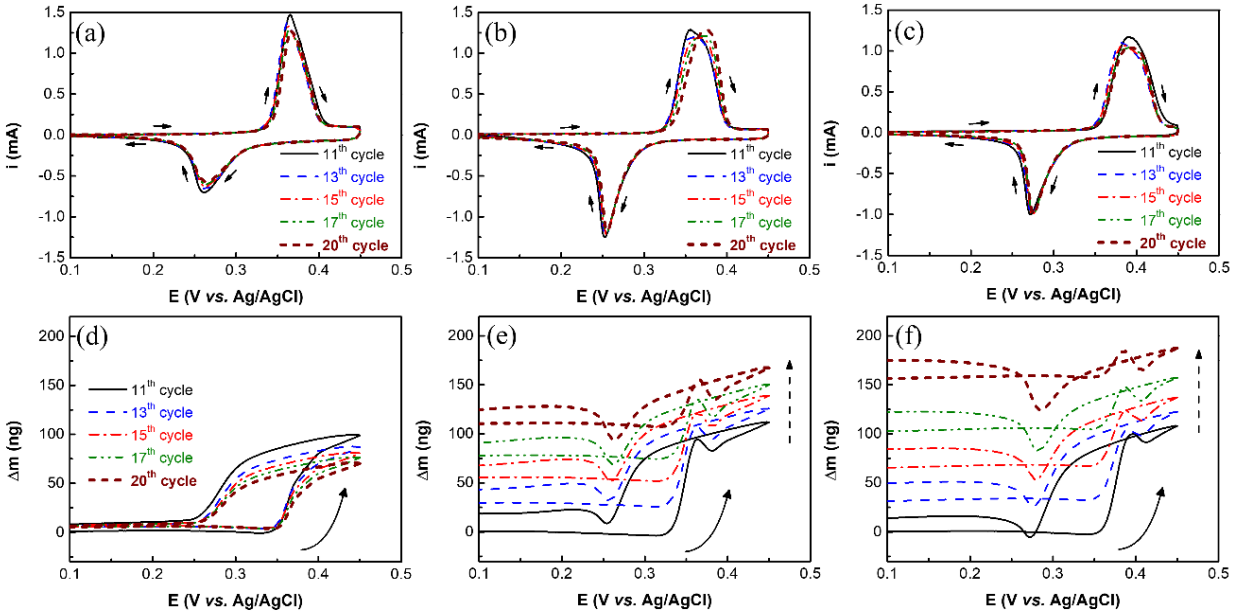

Figure 4 (a–c) cyclic voltammograms and (d–f) mass change profiles of α-$Ni(OH)_2(H_2O)$ deposited on EQCM gold electrodes for various cycles measured at 10 mV s^{-1} following 10 initial cycles at 5 mV s^{-1} (see Figures 3 and S3) in (a, d) in 1 M LiOH, (b, e) NaOH and (c, f) KOH. Values for Δm are referred to the accumulated mass at the beginning of 11th cycle.

occurrence of the phase transformation and ensuing electrochemical aging of the material. By measuring the change in the magnitude of the massograms peaks with cycling, the rate of phase transformation from γ/α to β/β is the fastest by means of potential cycling in KOH, while the absence of β/β signal for LiOH demonstrates the best retention ability. These results indicate that the $Ni(OH)_2$ phase transformation is strongly dependent on the electrolyte cation species with the degradation rate decreasing as $K^+ > Na^+ > Li^+$, in agreement with the general trend as observed for the *in situ* Raman spectroscopic results.

3.6 DFT-energy assisted EQCM stoichiometric resolution during cycling.

The results in the previous two Sections demonstrate that the degradation of the α phase takes place during the first 10 cycles only when the material is cycled in either NaOH or KOH. However, owing to the stoichiometry of the redox process, the EQCM measurements and the mass and charge balance equations (2)-(3) cannot provide any unambiguous quantitative insight on the change of stoichiometry (x,y,z) for the electroactive material during cycle, leaving the atomistic mechanisms of the degradation unquantified.

Below we illustrate a procedure to efficiently sample and screen, on a DFT-energy basis, the complete set of stoichiometric coefficients (x, y, z) that are solution to the mass and charge balance equations (2)-(3) for different electrochemical cycling. The advantage of available EQCM measurements is self-evident in that DFT energy screening of the possible stoichiometry for the electroactive material during cycling does not need to be carried out for any arbitrary composition in Eq. (1). Instead, it is limited only to those stoichiometric coefficients (x, y, z) that are compatible with the EQCM measurements, greatly reducing the sampling and computational efforts.

3.6.1 Initial oxidative charging

Figure 5a and **5b** shows the (infinite) possible solutions for *y* and *x/y*, respectively, as a function of the number of protons *z* that are compatible, via Eqs. (2)-(3), with the

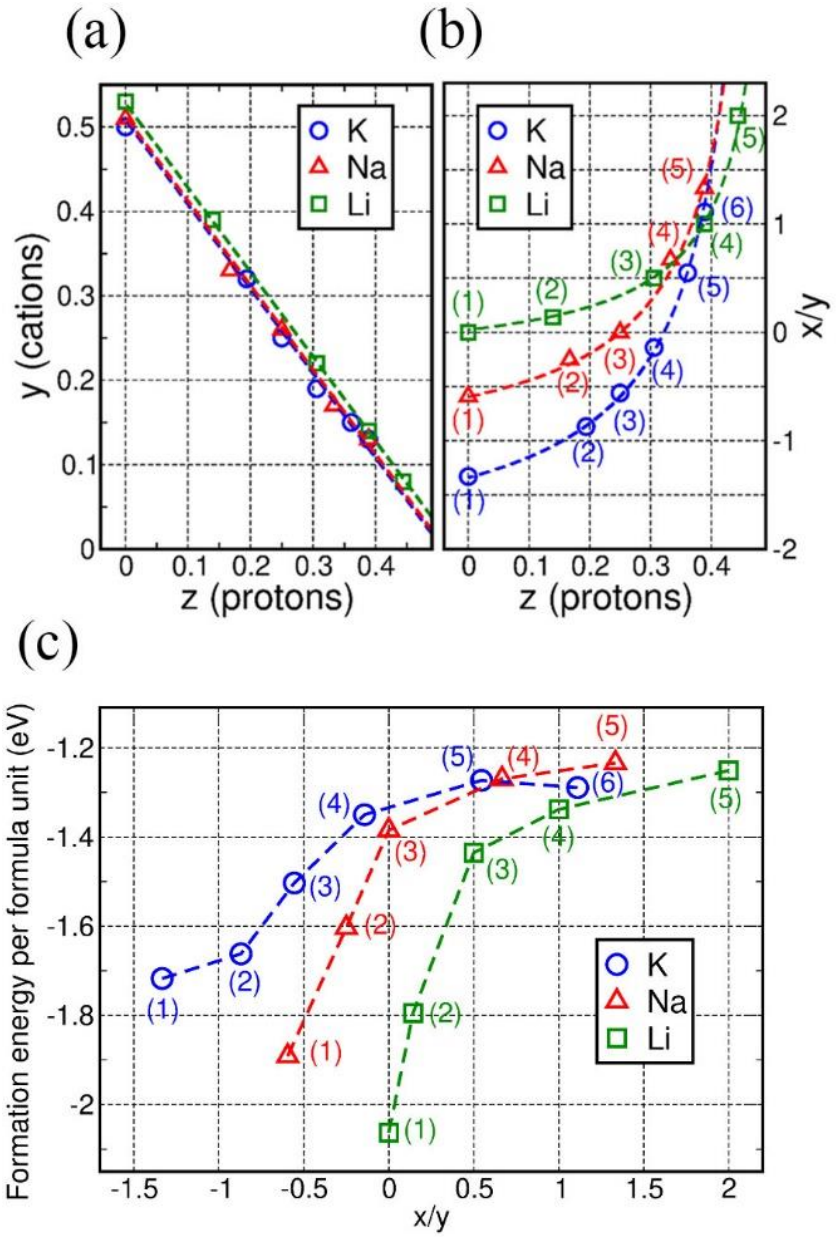

Figure 5 The EQCM-derived (infinite) possible solutions (dashed lines) for (a) the stoichiometric coefficients of cations (*y*), and (b) the water/cation (*x/y*) ratio as a function of the amount of protons (z) in γ-$M_yH_z(H_2O)_{1+x}NiO_2$ ($M=Li^+$, Na^+, K^+) following the first charge process. The empty symbols mark the stoichiometries used for the DFT-energy screening. The bracketed numbers label the models as in Table S6. (c) Computed DFT formation energies per formula unit of NiO_2 as a function of the water/cation (*x/y*) ratio. Same labelling as in (b).

measured Δm and Δq values for α-$Ni(OH)_2(H_2O)$ during the first oxidation. It is worth noting that since the α→γ oxidation requires intercalation of cations [M^+ in Eq. (1)] of stoichiometric coefficient y, we discarded any negative solution for y (y<0). Consistent with this choice, the sampling of z (the stoichiometric coefficient for protons, H^+, inside the γ phase in Eq. 1) was limited to the range between 0 (no protons inside the γ phase) and ~0.5 (largest z compatible with a y>0 value).

In contrast to chemical intuition, negative values of *x/y* (*x<0, y>0*) are also possible solutions to the system of equations (2)-(3). Note that, since *y>0*, a negative value of the *x/y* ratio indicates that *x* moles of structural water in the pristine α-$Ni(OH)_2(H_2O)$ are substituted by *y* moles of intercalated cations during the oxidation (charging) process. That is, cation intercalation displaces structural water inside the host. Surprisingly, this regime of perhaps counter-intuitive, yet mathematically sound, solutions to Eqs. (2)-(3) has so far been overlooked in the specialized literature.

By selecting 5-6 stoichiometries (symbols in **Figure 5**) among the infinite possible solutions of the mass and charge balance equations (**Eqs. 2-3**) for the first oxidation cycle, it is possible to define corresponding atomistic models for γ-$M_yH_z(H_2O)_{1+x}NiO_2$ (see Section S8 in the SI for details). Computed DFT formation energies for these models as a function of *x/y* (**Figure 5c**) reveal that, regardless of the electrolyte, the energetically favored stoichiometries correspond to *z = 0* and the lowest possible *x/y* ratio (Li^+: 0, Na^+: -0.6, K^+: -1.34). These results suggest that whereas insertion of Li^+ ions occurs without H_2O removal from the α-$Ni(OH)_2(H_2O)$ host, displacement of structural H_2O from the

host during intercalation of Na^+ and K^+ ions is energetically favored. They also indicate that full deprotonation upon charging (z=0 in Eq. 1) is energetically favored. Identification of the energy favored stoichiometric coefficients x, y, and z following the first oxidation, leads directly to the atomistic mechanism for the first charging process, that is presented in detail in Section S9 of the SI.

It is worth noting that, in spite of the different voltage scan rate (5 mV s^{-1} here, 10 mV s^{-1} in Ref. [5]), negative *x/y* ratios are solution *also* to the charge and mass balance equations for the EQCM measurements in Ref. [5] (refer to Figure 4 in Ref. 5). However, such a range of solution was overlooked as deemed electrochemically unsound.[5] The existence of negative x/y solutions for two set of EQCM experiments acquired with different voltage scan rates indirectly suggests that, at least qualitatively, the mechanism for ion intercalation in the two set of experiments should be similar with a contained role for kinetics aspects. Detailed analysis of the EQCM results for two different voltage scan rates (5 and 10 mV s^{-1}, **Figure S7 to S11** in the SI) reiterates this point.

3.6.2 Initial discharge and successive charge-discharge cycles

In principle, DFT-energy screening of the solutions compatible with EQCM measurements and charge and mass balance equations can be applied also to the reductive discharge from the γ to the α phase and successive γ/α electrochemical cycling.

In practice, however, the task is complicated by two factors. First, the lack of atomically-resolved characterization of the sample at each cycle prevents direct quantification of the amount of electroactive material participating in the (de)intercalation reaction [needed in Eqs. (2)-(4)]. Second, as shown by the EQCM measurements in **Figure 4** and Section S6 in the SI, the redox processes studied are not fully reversible. Such partial reversibility, manifesting in different mass and charge changes between oxidation and reduction, leads to an overall accumulation of material upon cycling. As a result, strictly, we lack of a fully quantitative way to determine both the amount of moles involved in the reaction [Eq. (4)] and differences in the moles of active material between oxidation and reduction. Although the measured Coulomb Efficiency (CE, Table S3) in the 85-68% range is noticeably lower than 100%, it changes by no more than 8% between consecutive cycles (KOH cycle 10 to 11 in Table S3), in line with the trends visible in Fig. S7 and S8 for the same electrochemical cycles.

Given the complexity of the problem, and the contained changes of CE between consecutive cycles, to a first approximation we opted for a conservative description and assumed that **(i)** the amount of moles (n) of the electroactive material remains the same during cycling. That is, the residual accumulated mass following one charge-discharge cycle (Figure S10 in the SI) remains in the charged γ-phase and, accordingly, does not participate in the next oxidative process. **(ii)** Charges responsible for the charge and discharge processes are the same (i.e. no current leakage is present), and **(iii)** as per Eqn. (1), the computed x/y ratio following the previous oxidation is maintained during the reduction process. We

refer the interested reader to Section S10 in the SI for an extensive description of the iterative procedure used to define the stoichiometry of the electroactive material during the first six charge-discharge cycles. Finally, to reduce the computational costs, and based on the calculated energy favorability of the absence of protons ($z = 0$) inside the γ phase following oxidation (**Figure. 5c**), a z=0 coefficient was used for all the models of the charged γ phase at successive electrochemical cycles.

Figure 6a shows the energetically favored stoichiometries for the charged γ phase. Although the amount of intercalated Li^+ ions (y) increases with the cycle number, the amount of structural water (x) remains practically unchanged. Conversely, for Na^+ and K^+ ions, the increase in intercalated ions (y) with cycle number is accompanied by a parallel reduction of structural water (x) in the host structure. The computed effect is larger going from Na^+ to K^+ ions.

Figure 6b shows the energetically favored stoichiometries for the discharged α phase as a function of the cycle number. The amount of residual hosted cations (y) increases with the cycle number. Increase of the cation content (y) is accompanied by reduction in the amount of protons (z) in the host materials. Whereas the amount of structural water (x) remains practically the same for Li^+ during electrochemical cycling, it gradually decreases for Na^+ and K^+. The progressive increase in the number of intercalated cations (y) is balanced by a decrease in the amount of protons (z) in order to maintain the average nickel

oxidation state equal to two. This feature further demonstrates that charge/discharge of the γ/α couple in NaOH and KOH electrolytes is not completely reversible.

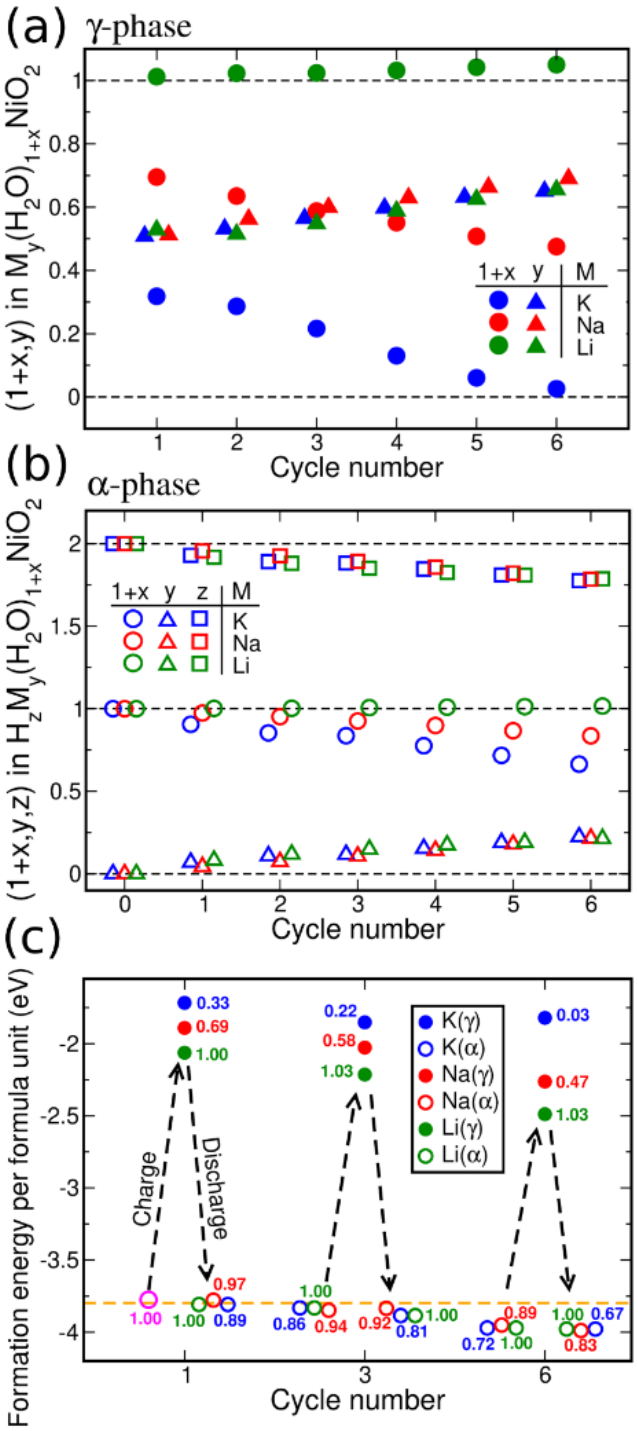

Figure 6 Energy-favored stoichiometries for (a) charged γ-$M_y(H_2O)_{1+x}NiO_2$ and (b) discharged α-$H_zM_y(H_2O)_{1+x}NiO_2$ for the first six cycles. M= Li^+, Na^+ or K^+. (c) Formation energy per formula unit at charged (filled symbols) and discharged (empty symbols) states for the 1st, 3rd and 6th cycle. The numerical labels (0.03 to 1.03) indicate the energy-favored amount of structural water (1+*x*) in the host structure. The magenta empty circle and the dashed orange line mark the formation energy of the pristine α-$Ni(OH)_2$ (H_2O) and β-$Ni(OH)_2$, respectively.

The computed lowest formation energy per formula unit for the first, third and sixth cycles are shown in **Figure 6c**. Formation energies for the initial charged γ state are lowest for insertion of Li^+ and highest for K^+, with intermediate values for Na^+. This trend is maintained for all the cycles considered.

Turning to the discharged α state, the formation energy of the structure containing Li^+ remains practically constant due to the similar content of residual Li^+. On the other hand, the formation energy decreases gradually with the cycle number for Na^+ and K^+, due to the increase of residual cations (*y*) in the structure (**Figure 6b**). The *x/y* ratio remains practically equal to zero for Li^+, while it gradually increases for Na^+ and K^+ with the cycle number (see **Figure S17a**). Moreover, the energy-favored stoichiometries of the charged states indicate a tendency for the average oxidation state of nickel atoms to be reduced with the cycle number (see **Figure S17b**). This is due to a loss in capacity for the material as the measured accumulated charge decreases with the cycle number (see Table S3 and Figure S8).

Although the DFT modelling has been carried out resting on the aforementioned assumption (i)-(iii), the energy favorability of progressive cation-induced water displacement with cycling is clearly visible, pointing to irreversible removal of structural water being the dominant factor in the degradation and aging of the α-phase. Furthermore, the presented EQCM-compliant DFT results clearly demonstrate that, pending the approximation used (Section S10 in the Supporting

Information), the EQCM-measured mass-changes do not match the amount of ions intercalated. Instead, they include also the amount of H^+ and structural H_2O displaced, in an irreversible manner, by the intercalation process.

SEM images take of the deposited $Ni(OH)_2$ onto the EQCM Au quartz crystal are shown in **Figure S18**. Little variation in morphology is observed on the pristine coating, however severe cracks are observable after cycling in all LiOH, NaOH, and KOH media, which is caused by the generated shear stress upon volume change during potential cycling. These results are in line with the calculated progressively larger structural changes between the γ and α phases going from LiOH to NaOH, to KOH (**Figure S19**).

3.6.3 Amended redox phase diagram for $Ni(OH)_2$

Based on the experimental and computational results, we propose a modified version of the Bode diagram for the different phases of $Ni(OH)_2$ (**Figure 1b**). Starting with the γ/α redox couple, first the solvated cations are driven to the electrode surface under the applied potential. Second, the hydration sphere of water molecules around the alkali metal cation is stripped away prior to insertion into the host structure, as previously suggested by Cheek *et al*.[52] Third, the inserted cations induce the displacement of structural water molecules from the inter-layer region, accompanied by removal of all the protons (H^+) from the host to form water (following combination with available OH^-). Conversely, the

mechanism for reduction process is proposed to take place through the removal of cations from the host structure followed by the re-insertion of water molecules into the inter-layer regions of the host.

Overall, the experimental and DFT results leads to the conclusion that the stability of the γ/α redox couple is governed by the retention of structural water following electrochemical (de)intercalation of cations. As detailed above, such retention is found to be strongly dependent on the nature of the intercalated cation, that is, electrolyte used. On this basis, the structural water molecules between the α–$Ni(OH)_2$ layers can be seen as an 'amorphous glue' needed to preserve the stability of the randomly stacked α phase structure.[22] Therefore, removal of structural water molecules from the α-$Ni(OH)_2$ structure during the charge/discharge process appears to be the driving factor for the phase transformation (aging) into the β-$Ni(OH)_2$ phase.

Since the water content inside the host structure remains almost unchanged following insertion/removal of Li^+ in the first six cycles, the stability of the γ/α redox couple in LiOH is larger with respect to (structural water displacing) NaOH and KOH electrolytes.

At the charged γ state in the sixth cycle, the amount of structural water in the host (x) is reduced to 0.47 for Na^+ and to almost zero for K^+ (0.03, **Figure 6c**). Clearly, if water molecules cannot be re-inserted back quickly enough into the nickel structure once the cations are removed, the structure will be prone to collapse, leading to the transformation into the β $Ni(OH)_2$ phase. Consistent with the larger amount of water displaced from the host, degradation is found to be more severe as the cation size and

cation to removed water ratio (x/y in Fig. S17) increases. Based on these results, synthetic routes to 3D-porous (rather than layered) $Ni(OH)_2$ substrates or exploration of hydrogen-bonding forming agents, chemically or electrochemically inserted among $Ni(OH)_2$ layers to prevent their collapse, emerge as potentially rewarding directions for follow up studies.

4. CONCLUSIONS

By development and application of a new approach combining *in situ* Raman and DFT-energy assisted interpretation of EQCM measurements, we have investigated the changes in stoichiometry, and ensuing degradation, for α-$Ni(OH)_2(H_2O)$ during electrochemical cycling in different LiOH, NaOH, KOH electrolytes. Quantitative resolution of the stoichiometric changes for the electroactive material during cycling enables unambiguous identification of a hitherto overlooked mechanism leading to displacement of structural water and protons from the layered host upon electrochemical intercalation of the electrolyte cation. The partially irreversible nature of the redox process leads to progressive depletion of structural water from the host upon continued cycling, promoting the collapse of the pristine α structure into the electrochemically less active β phase. Due to the larger amount of water displaced from the host per intercalated ion, the degradation process is found to become faster and more severe as the size of the electrolyte cation increases ($Li^+ < Na^+ < K^+$). The presented experimental and computational results significantly extend the available atomistic understanding of electrochemical phase transformations of α-$Ni(OH)_2(H_2O)$, pointing the way for new research in improved solutions based on stabilization of the substrate. We anticipate the new approach presented, findings, and generated insight to be readily transferable to the research in electrochemical applications and, more generally, to the many ion-intercalation hosts presently investigated for electrochemical energy storage and conversion applications.

ACKNOWLEDGMENTS

We would like to acknowledge the support of the European Commission FP7 Project “Stable Interfaces for Rechargeable Batteries” (SIRBATT) (FP7-ENERGY-2013, grant agreement No. 608502), the Royal Society and the Engineering and Physical Sciences Research Council (EPSRC) for the part funding of this research under Grant Number EP/I004483/1 (GT) and EP/N032888/1 (LJH). LJH further acknowledges the partial support of ISCF Faraday Challenge project: “Quantitative Imaging of Multi-Scale Dynamic Phenomena at Electrochemical Interfaces” under grant number EP/T007745/1. The Ministry of Science and Technology, Taiwan (MOST 103-2911-I-007-515, 104-2911-I-007-504, 105-2221-E-007-127-MY3) and the boost program (106N510CE1) in the LCERC of National Tsing Hua University (NTHU) is acknowledged. Ivan Scivetti acknowledges CCP5 funding and associated CoSeC support at STFC. The experimental work was carried out within the cooperative framework set-up between NTHU, Taiwan and University of Liverpool, UK. This work made use of the HPC Wales, ARCHER (via the UKCP Consortium, EPSRC UK EP/K013610/1, EP/P022189/1 and EP/P022189/2) and STFC Scientific Computing Department's SCARF High-Performance Computing facilities. Yi-Ting Lu is acknowledged for assistance in measuring $Ni(OH)_2$ baseline Raman spectra.

ASSOCIATED CONTENT

Supporting Information. "This material is available free of charge via the Internet at http://pubs.acs.org." PXRD pattern of as-prepared samples; pH effect of alkaline media; EQCM results and analysis; Traces of α to β aging; Composition of pristine $Ni(OH)_2$ samples; Further computational details; Proposed stoichiometry for the first oxidation; Complementary *in situ* Raman spectra

AUTHOR INFORMATION

THW, JAW carried out the experiments. THW, IS, JAW, GT, CCH, and LJH analyzed the EQCM and Raman experiments. IS set up, executed and analyzed the DFT simulations. THW, IS and GT wrote the first manuscript of the paper. All the authors contributed to the final version of the paper. CCH and LJH designed the experimental research strategy. IS developed conceptually and computationally the presented DFT-EQCM protocol for stoichiometry resolution during cycling.

REFERENCES

(1) Armand, M.; Tarascon, J. M. Building Better Batteries. *Nature* **2008,** *451*, 652-657.

(2) Winter, M.; Besenhard, J. O.; Spahr, M. E.; Novák, P. Insertion Electrode Materials for Rechargeable Lithium Batteries. *Adv. Mater.* **1998,** *10*, 725-763.

(3) Cheng, F.; Liang, J.; Tao, Z.; Chen, J. Functional Materials for Rechargeable Batteries. *Adv. Mater.* **2011,** *23*, 1695-1715.

(4) Mo, Y.; Hwang, E.; Scherson, D. A. *In Situ* Quartz Crystal Microbalance Studies of Nickel Hydrous Oxide Films in Alkaline Electrolytes. *J. Electrochem. Soc.* **1996,** *143*, 37-43.

(5) Cordoba-Torresi, S. I.; Gabrielli, C.; Hugot-Le Goff, A.; Torresi, R. Electrochromic Behavior of Nickel Oxide Electrodes. I. Identification of the Colored State Using Quartz Crystal Microbalance. *J. Electrochem. Soc.* **1991,** *138*, 1548-1553.

(6) Kim, M. S.; Hwang, T. S.; Kim, K. B. A Study of the Electrochemical Redox Behavior of Electrochemically Precipitated Nickel Hydroxides Using Electrochemical Quartz Crystal Microbalance. *J. Electrochem. Soc.* **1997,** *144*, 1537-1543.

(7) Kim, M. S.; Kim, K. B. A Study on the Phase Transformation of Electrochemically Precipitated Nickel Hydroxides Using an Electrochemical Quartz Crystal Microbalance. *J. Electrochem. Soc.* **1998,** *145*, 507-511.

(8) Wehrens-Dijksma, M.; Notten, P. H. L. Electrochemical Quartz Microbalance Characterization of $Ni(OH)_2$-Based Thin Film Electrodes. *Electrochim. Acta* **2006,** *51*, 3609-3621.

(9) Reisner, D. E.; Salkind, A. J.; Strutt, P. R.; Xia, T. D. Nickel Hydroxide and Other Nanophase Cathode Materials for Rechargeable Batteries. *J. Power Sources* **1997,** *65*, 231-233.

(10) Hu, W. K.; Noréus, D. Alpha Nickel Hydroxides as Lightweight Nickel Electrode Materials for Alkaline Rechargeable Cells. *Chem. Mater.* **2003,** *15*, 974-978.

(11) Chen, J.; Cheng, F. Combination of Lightweight Elements and Nanostructured Materials for Batteries. *Acc. Chem. Res.* **2009,** *42*, 713-723.

(12) Wang, H.; Casalongue, H. S.; Liang, Y.; Dai, H. $Ni(OH)_2$ Nanoplates Grown on Graphene as Advanced Electrochemical Pseudocapacitor Materials. *J. Am. Chem. Soc.* **2010,** *132*, 7472-7477.

(13) Yan, J.; Fan, Z.; Sun, W.; Ning, G.; Wei, T.; Zhang, Q.; Zhang, R.; Zhi, L.; Wei, F. Advanced Asymmetric Supercapacitors Based on $Ni(OH)_2$/Graphene and Porous Graphene Electrodes with High Energy Density. *Adv. Funct. Mater.* **2012,** *22*, 2632-2641.

(14) Hu, C. C.; Chen, J. C.; Chang, K. H. Cathodic Deposition of $Ni(OH)_2$ and $Co(OH)_2$ for Asymmetric Supercapacitors: Importance of the Electrochemical Reversibility of Redox Couples. *J. Power Sources* **2013,** *221*, 128-133.

(15) Wei, D.; Scherer, M. R.; Bower, C.; Andrew, P.; Ryhanen, T.; Steiner, U. A Nanostructured

Electrochromic Supercapacitor. *Nano Lett.* **2012,** *12*, 1857-1862.

(16) Bouessay, I.; Rougier, A.; Poizot, P.; Moscovici, J.; Michalowicz, A.; Tarascon, J. M. Electrochromic Degradation in Nickel Oxide Thin Film: A Self-Discharge and Dissolution Phenomenon. *Electrochim. Acta* **2005,** *50*, 3737-3745.

(17) Xia, X. H.; Tu, J. P.; Zhang, J.; Wang, X. L.; Zhang, W. K.; Huang, H. Electrochromic Properties of Porous NiO Thin Films Prepared by a Chemical Bath Deposition. *Sol. Energy Mater. Sol. Cells* **2008,** *92*, 628-633.

(18) Xu, L.; Ding, Y. S.; Chen, C. H.; Zhao, L.; Rimkus, C.; Joesten, R.; Suib, S. L. 3D Flowerlike α-Nickel Hydroxide with Enhanced Electrochemical Activity Synthesized by Microwave-Assisted Hydrothermal Method. *Chem.Mater.* **2008,** *20*, 308-316.

(19) Subbaraman, R.; Tripkovic, D.; Chang, K. C.; Strmcnik, D.; Paulikas, A. P.; Hirunsit, P.; Chan, M.; Greeley, J.; Stamenkovic, V.; Markovic, N. M. Trends in Activity for the Water Electrolyser Reactions on 3d M(Ni,Co,Fe,Mn) Hydr(oxy)oxide Catalysts. *Nat. Mater.* **2012,** *11*, 550-557.

(20) Trotochaud, L.; Young, S. L.; Ranney, J. K.; Boettcher, S. W. Nickel-Iron Oxyhydroxide Oxygen-Evolution Electrocatalysts: the Role of Intentional and Incidental Iron Incorporation. *J. Am. Chem. Soc.* **2014,** *136*, 6744-6753.

(21) Bode, H.; Dehmelt, K.; Witte, J. Zur Kenntnis der Nickelhydroxidelektrode—I. Über das Nickel (II)-Hydroxidhydrat. *Electrochim. Acta* **1966,** *11*, 1079-1087.

(22) McEwen, R. S. Crystallographic Studies on Nickel Hydroxide and the Higher Nickel Oxides. *J. Phys. Chem.* **1971,** *75*, 1782-1789.

(23) Oliva, P.; Leonardi, J.; Laurent, J. F., Review of the Structure and the Electrochemistry of Nickel Hydroxides and Oxyhydroxides. *J. Power Sources* **1982,** *8*, 229-255.

(24) Kamath, P. V.; Dixit, M.; Indira, L.; Shukla, A. K.; Kumar, V. G.; Munichandraiah, N. Stabilized α-$Ni(OH)_2$ as Electrode Material for Alkaline Secondary Cells *J. Electrochem. Soc.* **1994,** *141*, 2956-2959.

(25) Kim, M. S.; Kim, K. B. A Study on the Phase Transformation of Electrochemically Precipitated Nickel Hydroxides Using an Electrochemical Quartz Crystal Microbalance. *J. Electrochem. Soc.* **1998,** *145*, 507-511.

(26) Kim, M. S.; Hwang, T. S.; Kim, K. B. A Study of the Electrochemical Redox Behavior of Electrochemically Precipitated Nickel Hydroxides Using Electrochemical Quartz Crystal Microbalance. *J. Electrochem. Soc.* **1997,** *144*, 1537-1543.

(27) Bernard, M. C.; Bernard, P.; Keddam, M.; Senyarich, S.; Takenouti, H. Characterization of New Nickel Hydroxides during the Transformation of α-$Ni(OH)_2$ to β-$Ni(OH)_2$ by Aging. *Electrochimica acta* **1996,** *41*, 91-93.

(28) Delahaye-Vidal, A.; Sac-Epée, N.; Tekaia-Elhsissen, K.; Audemer, A.; Figlarz, M. Structural and Textural Investigations of the Nickel Hydroxide Electrode. *Solid State Ionics* **1996,** *84*, 239-248.

(29) Hu, C. C.; Chen, W. C., Effects of Substrates on the Capacitive Performance of $RuO_x \cdot nH_2O$ and Activated Carbon–RuO_x Electrodes for Supercapacitors. *Electrochim. Acta* **2004,** *49*, 3469-3477.

(30) Yang, D.; Wang, R.; He, M.; Zhang, J.; Liu, Z. Ribbon- and Boardlike Nanostructures of Nickel Hydroxide Synthesis, Characterization, and Electrochemical Properties. *J. Phys. Chem. B* **2005,** *109*, 7654-7658.

(31) Blöchl, P. E. Projector Augmented-Wave Method. *Phys. Rev. B* **1994,** *50*, 17953-17979.

(32) Kresse, G.; Furthmüller, J. Efficiency of *Ab-Initio* Total Energy Calculations for Metals and Semiconductors Using a Plane-Wave Basis Set. *Comput. Mater. Sci.* **1996,** *6*, 15-50.

(33) Kresse, G.; Furthmüller, J. Efficient Iterative Schemes for *Ab Initio* Total-Energy Calculations Using a Plane-Wave Basis Set. *Phys. Rev. B* **1996,** *54*, 11169-11186.

(34) Kresse, G.; Joubert, D. From Ultrasoft Pseudopotentials to the Projector Augmented-Wave Method. *Phys. Rev. B* **1999,** *59*, 1758-1775.

(35) Van der Ven, A.; Morgan, D.; Meng, Y. S.; Ceder, G. Phase Stability of Nickel Hydroxides and Oxyhydroxides. *J. Electrochem. Soc.* **2006,** *153*, A210-A215.

(36) Wang, Y.; Perdew, J. P. Correlation Hole of the Spin-Polarized Electron Gas, with Exact Small-Wave-Vector and High-Density Scaling. *Phys. Rev. B* **1991,** *44*, 13298-13307.

(37) Vosko, S. H.; Wilk, L.; Nusair, M. Accurate Spin-Dependent Electron Liquid Correlation Energies for Local Spin Density Calculations a Critical Analysis. *Can. J. Phys.* **1980,** *58*, 1200-1211.

(38) Anisimov, V. I.; Zaanen, J.; Andersen, O. K. Band Theory and Mott Insulators: Hubbard *U* Instead of Stoner *I*. *Phys. Rev. B* **1991,** *44*, 943-954.

(39) Anisimov, V. I.; Solovyev, I. V.; Korotin, M. A.; Czyżyk, M. T.; Sawatzky, G. A. Density-Functional Theory and NiO Photoemission Spectra. *Phys. Rev. B* **1993,** *48*, 16929-16934.

(40) Cococcioni, M.; de Gironcoli, S. Linear Response Approach to the Calculation of the Effective Interaction Parameters in the LDA+U Method. *Phys. Rev. B* **2005,** *71*.

(41) Himmetoglu, B.; Floris, A.; de Gironcoli, S.; Cococcioni, M. Hubbard-Corrected DFT Energy Functionals: The LDA+U Description of Correlated Systems. *Int. J. Quantum Chem.* **2014,** *114*, 14-49.

(42) Dudarev, S. L.; Botton, G. A.; Savrasov, S. Y.; Humphreys, C. J.; Sutton, A. P. Electron-Energy-Loss Spectra and the Structural Stability of Nickel Oxide: An LSDA+U Study. *Phys. Rev. B* **1998,** *57*, 1505-1509.

(43) Zaffran, J.; Caspary Toroker, M. Benchmarking Density Functional Theory Based Methods To Model NiOOH Material Properties: Hubbard and van der Waals Corrections vs Hybrid Functionals. *J. Chem. Theory Comput.* **2016,** *12*, 3807-3812.

(44) Monkhorst, H. J.; Pack, J. D. Special Points for Brillouin-Zone Integrations. *Phys. Rev. B* **1976,** *13*, 5188-5192.

(45) Momma, K.; Izumi, F. *VESTA 3* for Three-Dimensional Visualization of Crystal,

Volumetric and Morphology Data. *J. Appl. Crystallogr.* **2011,** *44*, 1272-1276.

(46) Hall, D. S.; Lockwood, D. J.; Poirier, S.; Bock, C.; MacDougall, B. R. Raman and Infrared Spectroscopy of Alpha and Beta Phases of Thin Nickel Hydroxide Films Electrochemically Formed on Nickel. *J. Phys. Chem. A* **2012,** *116*, 6771-6784.

(47) Hall, D. S.; Lockwood, D. J.; Poirier, S.; Bock, C.; MacDougall, B. R. Applications of *In Situ* Raman Spectroscopy for Identifying Nickel Hydroxide Materials and Surface Layers during Chemical Aging. *ACS Appl. Mater. Interfaces* **2014,** *6*, 3141-3149.

(48) Hall, D. S.; Lockwood, D. J.; Bock, C.; MacDougall, B. R. Nickel Hydroxides and Related Materials: a Review of Their Structures, Synthesis and Properties. *Proc. Math. Phys. Eng. Sci.* **2015,** *471*, 20140792.

(49) Faure, C.; Delmas, C.; Fouassier, M. Characterization of a Turbostratic α-Nickel Hydroxide Quantitatively Obtained from an $NiSO_4$ Solution. *J. Power Sources* **1991,** *35*, 279-290.

(50) Mo, Y.; Hwang, E.; Scherson, D. A. *In Situ* Quartz Crystal Microbalance Studies of Nickel Hydrous Oxide Films in Alkaline Electrolytes. *J. Electroanal. Soc.* **1996,** *143*, 37-43.

(51) Hu, C. C.; Chang, K. H.; Hsu, T. Y. The Synergistic Influences of OH^- Concentration and Electrolyte Conductivity on the Redox Behavior of $Ni(OH)_2$/NiOOH. *J. Electrochem. Soc.* **2008,** *155*, F196-F200.

(52) Cheek, G. T.; O'Grady, W. E. Redox Behavior of the Nickel Oxide Electrode System Quartz Crystal Microbalance Studies. *J. Electroanal. Chem.* **1997,** *421*, 173-177.

(53) Bernard, P.; Gabrielli, C.; Keddam, M.; Takenouti, H. Ac Quartz Crystal Microbalance Applied to the Studies of the Nickel Hydroxide Behavior in Alkaline Solutions. *Electrochim. Acta* **1991,** *36*, 743-746.

Table of content figure